ARTICLES
https://doi.org/10.1038/s41563-020-00880-6

nature materials

Highly luminescent and catalytically active suprastructures of magic-sized semiconductor nanoclusters

Woonhyuk Baek[1,2,4], Megalamane S. Bootharaju[1,2,4], Kelly M. Walsh[3], Sanghwa Lee[1,2], Daniel R. Gamelin[3] and Taeghwan Hyeon[1,2] ✉

Metal chalcogenide magic-sized nanoclusters have shown intriguing photophysical and chemical properties, yet ambient instability has hampered their extensive applications. Here we explore the periodic assembly of these nanoscale building blocks through organic linkers to overcome such limitations and further boost their properties. We designed a diamine-based heat-up self-assembly process to assemble Mn^{2+}:$(CdSe)_{13}$ and Mn^{2+}:$(ZnSe)_{13}$ magic-sized nanoclusters into three- and two-dimensional suprastructures, respectively, obtaining enhanced stability and solid-state photoluminescence quantum yields (from <1% for monoamine-based systems to ~72% for diamine-based suprastructures). We also exploited the atomic-level miscibility of Cd and Zn to synthesize Mn^{2+}:$(Cd_{1-x}Zn_xSe)_{13}$ alloy suprastructures with tunable metal synergy: Mn^{2+}:$(Cd_{0.5}Zn_{0.5}Se)_{13}$ suprastructures demonstrated high catalytic activity (turnover number, 17,964 per cluster in 6 h; turnover frequency, 2,994 per cluster per hour) for converting CO_2 to organic cyclic carbonates under mild reaction conditions. The enhanced stability, photoluminescence and catalytic activity through combined cluster-assembly and metal synergy advance the usability of inorganic semiconductor nanoclusters.

Colloidal semiconductor magic-sized nanoclusters (MSCs) are atomically defined, ultrasmall (<2 nm diameter) and metastable species frequently encountered in the synthesis of nanocrystals[1–7]. The growth of nanocrystals has often been identified to follow the non-classical growth mechanism, where the MSCs of discrete size sequentially form before the formation of the stable nanocrystals[3,8,9]. The MSCs are highly attractive because their atomic and electronic structure characterization provides valuable insights into the reaction control and fundamental understanding of the dynamics of nanocrystal formation[10]. The MSCs possess unique electronic structures[4,5,11], resulting in characteristic absorption and band-edge emission profiles[1,12–15], typical of strong size- and structure-induced quantum confinement[2,12,16]. The observed properties correspond to solely MSCs as they are single-sized with the precise chemical composition[17–21], distinct from the ensemble averages in nanocrystals[22,23], making MSCs more unique compared with the nanocrystals.

Crystalline materials constructed from the periodic arrangement of nanostructured building blocks, such as metal nanoclusters connected by organic linkers in metal–organic frameworks, have gained much attention for their potential applications, including gas storage, separation and catalysis[24,25]. Such hybrid materials of inorganic (metal nanoclusters) and organic (linkers) components provide not only high stability, but they also integrate the properties of the individual components[26]. Particularly, photoluminescence (PL) and catalytic efficiency have been found to be enhanced by several orders of magnitude by assembling metal chalcogenide or chalcogenolate nanoclusters[19,27–29]. Apart from the periodic arrangement of building blocks, the synergistic interactions between metal and ligand[27] (metal–ligand synergy) or two different metals[30] (metal synergy) play an important role in the enhancement of catalytic activity. Furthermore, the assembly of nanostructured building blocks, including monodispersed nanoparticles[31–35], by site-specific interactions is anticipated to overcome interfacial issues[36,37], which are prevalent in conventional hybrid composite materials prepared by physical mixing, resulting only in nominally enhanced properties.

The stoichiometric MSCs comprising 1:1 metal-to-chalcogenide ratios[5,12,38–40] are special cases of MSCs, whose synthesis and characterization are still challenging. Notable examples for the experimentally isolated stoichiometric MSCs are amine-ligated $(CdSe)_{13}$ (refs. [18,41]), $(ZnSe)_{13}$ (ref. [38]) and $(CdSe)_{34}$ (refs. [12,42]). The Mn^{2+}-related PL via the $^4T_1$–$^6A_1$ d–d transition has been realized in the smallest semiconductor MSCs $(CdSe)_{13}$ and $(ZnSe)_{13}$ by substitutional Mn^{2+} doping[38,43]. Furthermore, MSCs have served as precursors to high-dimensional nanostructures[6,39,42]. Nevertheless, the poor stability has severely hindered further advancement of MSCs towards optoelectronic and catalytic applications. Although Mn^{2+} doping of $(CdSe)_{13}$ enhances its stability slightly, its PL quantum yield (PLQY) remains unsatisfactory (see below), indicating the need for new strategies to enhance various properties of MSCs. Inspired by the ligand-based assembly of metal nanoclusters[28], here we develop a facile method to self-assemble Mn^{2+}-doped MSCs of $(CdSe)_{13}$, $(ZnSe)_{13}$ and their alloys into corresponding suprastructures (SSs), exhibiting much enhanced stability, PLQY and catalytic activity.

Ligand-denticity-directed formation of SSs

The nanostructured building blocks coordinated with multidentate ligands are anticipated to be self-assembled into ordered structures in a manner akin to coordination polymers and metal–organic frameworks[25,44]. Although adopting such ligand-based methodology

[1]Center for Nanoparticle Research, Institute for Basic Science (IBS), Seoul, Republic of Korea. [2]School of Chemical and Biological Engineering, and Institute of Chemical Processes, Seoul National University, Seoul, Republic of Korea. [3]Department of Chemistry, University of Washington, Seattle, WA, USA. [4]These authors contributed equally: Woonhyuk Baek, Megalamane S. Bootharaju. ✉e-mail: thyeon@snu.ac.kr

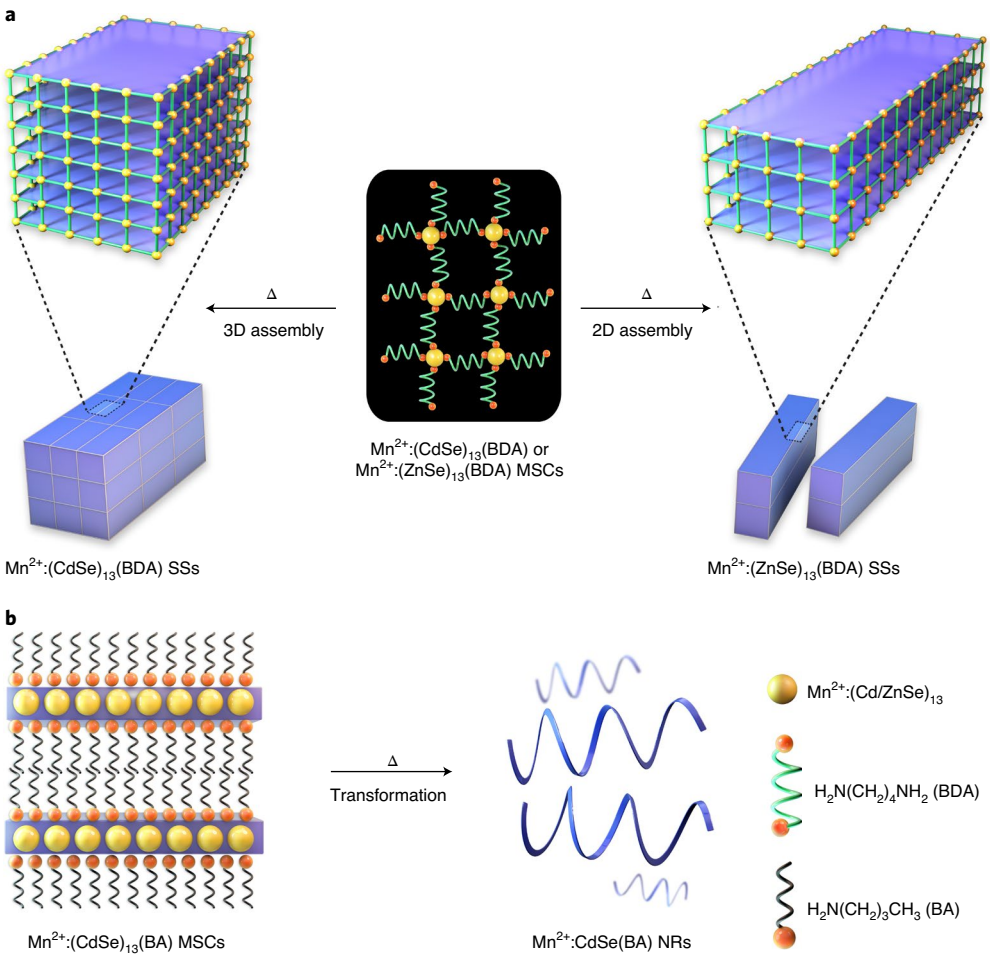

Fig. 1 | Schematic representation of the unique growth pathways of MSCs. a, Formation of self-assembled 3D Mn^{2+}:$(CdSe)_{13}$(BDA) (left) and 2D Mn^{2+}:$(ZnSe)_{13}$(BDA) SSs (right) from corresponding Mn^{2+}-doped MSCs upon colloidal thermal (Δ) treatment. **b**, High-temperature transformation of monoamine (BA)-ligated lamellar Mn^{2+}:$(CdSe)_{13}$(BA) MSCs to Mn^{2+}:CdSe(BA) NRs. The rigid binding of diamines favours the formation of SSs of intact MSCs, while its absence makes monoamines unable to stabilize MSCs, leading to their growth to NRs.

for assembling building blocks of metal chalcogenide MSCs seems simple, synthesizing MSCs with desired ligands is not trivial. In this study, Mn^{2+}-doped $(CdSe)_{13}$ and $(ZnSe)_{13}$ MSCs are synthesized by using *n*-butylamine (BA) and butane-1,4-diamine (BDA) as ligands, comprising identical carbon chain length yet differing by a single $–NH_2$ group. Upon colloidal thermal treatment, the bidentate BDA is found to assemble these MSCs into large SSs, while the monodentate BA fails to preserve the structure of MSCs and leads them to transform into nanoribbons (NRs) (Fig. 1), demonstrating that multidentate ligands are indeed capable of ordering nanobuilding blocks into higher-dimensional nanostructures. The rigid binding of diamines with MSCs, supported by high thermal stability (see below), facilitates the self-assembly of MSCs. Lack of such rigidity in monoamines and the resultant low stability under thermal conditions lead to the transformation of MSCs. While the two $–NH_2$ groups of diamine are vital for the SS formation, its carbon chain length is also found to substantially influence the degree of self-assembly of MSCs. Predominant hydrophobic interactions among long-chain diamines and extended intercluster separation lead to destabilization of MSCs, favouring their transformation to NRs. The optimal carbon chain length for the high degree of SS formation is found to be that of BDA (see below).

The synthesis of SSs of MSCs comprises two important steps. In the first step, Mn^{2+}-doped $(CdSe)_{13}$ and $(ZnSe)_{13}$ MSCs ligated with BDA, denoted as Mn^{2+}:$(CdSe)_{13}$(BDA) and Mn^{2+}:$(ZnSe)_{13}$(BDA), respectively, are synthesized via Lewis acid–base reactions between highly active Se (selenocarbamate) and metal (diamine complexes of $CdCl_2$ or $ZnCl_2$ and $MnCl_2$) precursors at room temperature (25 °C) (see Methods and Supplementary Fig. 1 for details). The reaction products, Mn^{2+}:$(CdSe)_{13}$ and Mn^{2+}:$(ZnSe)_{13}$ MSCs possess two-dimensional (2D) sheet-like morphology (Supplementary Fig. 2) similar to the reported monoamine ligated MSCs[39]. In the second step, these colloidal MSCs are heated to transform 2D sheets into 3D and 2D SSs of Mn^{2+}:$(CdSe)_{13}$(BDA) and Mn^{2+}:$(ZnSe)_{13}$(BDA) MSCs, respectively (Fig. 2 and Supplementary Fig. 3). The transmission electron microscopy (TEM) image of the Mn^{2+}:$(CdSe)_{13}$(BDA) SS shows that MSCs assemble to form large brick-like structures with the size range of 0.1–1.0 μm (Fig. 2a). The brick-like 3D stacks of SSs are seen in the field emission scanning electron microscopy (FESEM) and high-angle annular dark-field scanning TEM (HAADF-STEM) images with the thickness in the range of 0.08–0.3 μm (Supplementary Fig. 4). On the other hand, the Mn^{2+}:$(ZnSe)_{13}$(BDA) SSs show a 2D morphology with the length and thickness range of 0.3–0.8 and 0.03–0.15 μm, respectively (Fig. 2c and Supplementary Fig. 5).

Interestingly, upon heating of colloidal Mn^{2+}:$(CdSe)_{13}$(BA) MSCs, Mn^{2+}-doped CdSe NRs, denoted as Mn^{2+}:CdSe(BA) NRs, are formed by dissolution of MSCs in the growth solution. The TEM image in Fig. 2e shows Mn^{2+}:CdSe(BA) NRs with a thin 2D tangled structure. Upon similar heat treatment, Mn^{2+}:$(ZnSe)_{13}$(BA) MSCs produce

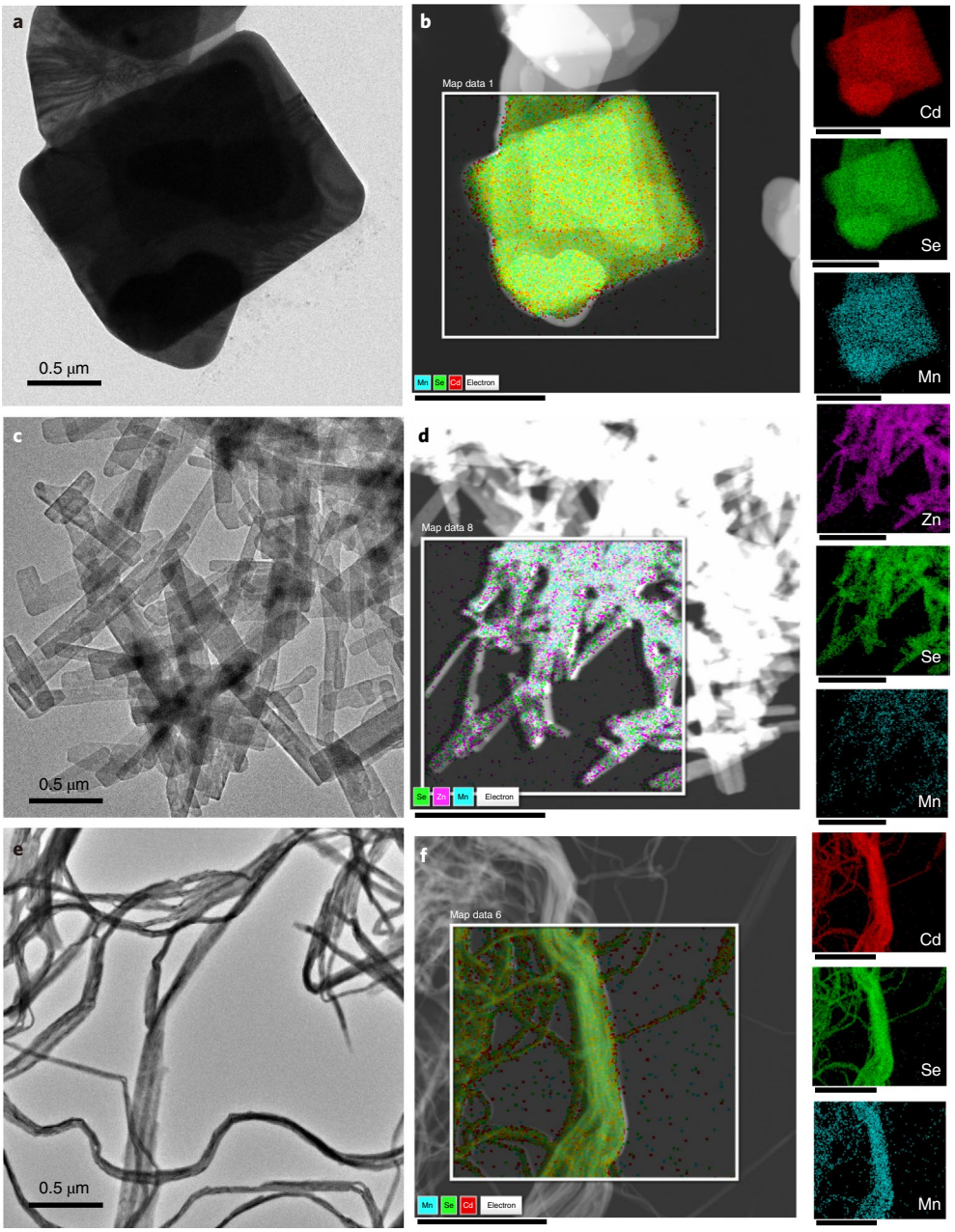

Fig. 2 | Morphology characterization of SSs of MSCs and NRs. a–f, TEM images (**a**,**c**,**e**) and HAADF-STEM images and EDS elemental maps (**b**,**d**,**f**) of SSs of Mn^{2+}:$(CdSe)_{13}$(BDA) (**a**,**b**) and Mn^{2+}:$(ZnSe)_{13}$(BDA) (**c**,**d**) and NRs of Mn^{2+}:CdSe(BA) (**e**,**f**). The scale bars in **b**,**d**,**f** and their elemental maps are 1 μm. The Mn^{2+}:$(CdSe)_{13}$(BDA) and Mn^{2+}:$(ZnSe)_{13}$(BDA) MSCs self-assemble into a square-like (**a**) and rectangle-like (**c**) morphology with considerable thickness. In contrast, the monoamine-ligated Mn^{2+}:$(CdSe)_{13}$(BA) MSCs transform to ultralong, thin NRs (**e**), demonstrating the crucial role of BDA and BA in the self-assembly and transformation of MSCs.

uncontrolled and indefinite Mn^{2+}:ZnSe nano/micro-structures (Supplementary Fig. 6). The HAADF-STEM energy dispersive X-ray spectroscopy (STEM-EDS) elemental mappings (Fig. 2b,d,f) reveal that these materials are composed of Cd (or Zn), Se and Mn elements with a homogeneous distribution throughout the structures. These results clearly indicate the critical role of diamines in the formation of SSs of intact MSC building blocks.

Optical properties

The absorption spectrum of Mn^{2+}:$(CdSe)_{13}$(BDA) MSCs shows two clear peaks at 353 and 340 nm, along with a broad peak at 305 nm (Fig. 3a). The characteristic Mn^{2+} PL at ~593 nm indicates the successful Mn^{2+} doping of the CdSe MSCs. The PL excitation (PLE) spectrum for the 593 nm Mn^{2+} emission matches very well with the absorption profile, confirming the presence of Mn^{2+} within the $(CdSe)_{13}$ cluster by Cd substitution as indicated by mass spectrometry results (Supplementary Fig. 3). The Mn^{2+}:$(CdSe)_{13}$(BDA) SSs do not show the signature features of MSCs in their colloidal-state absorption spectrum due to the micrometre-sized particles and resultant predominant light scattering. However, their solid-state diffuse reflectance spectrum clearly manifests the absorption features of MSCs (Supplementary Fig. 7). The solid-state absorption, PL, PLE and mass spectra of SSs are very similar to those of Mn^{2+}:$(CdSe)_{13}$(BDA) MSCs, strongly suggesting that the SSs

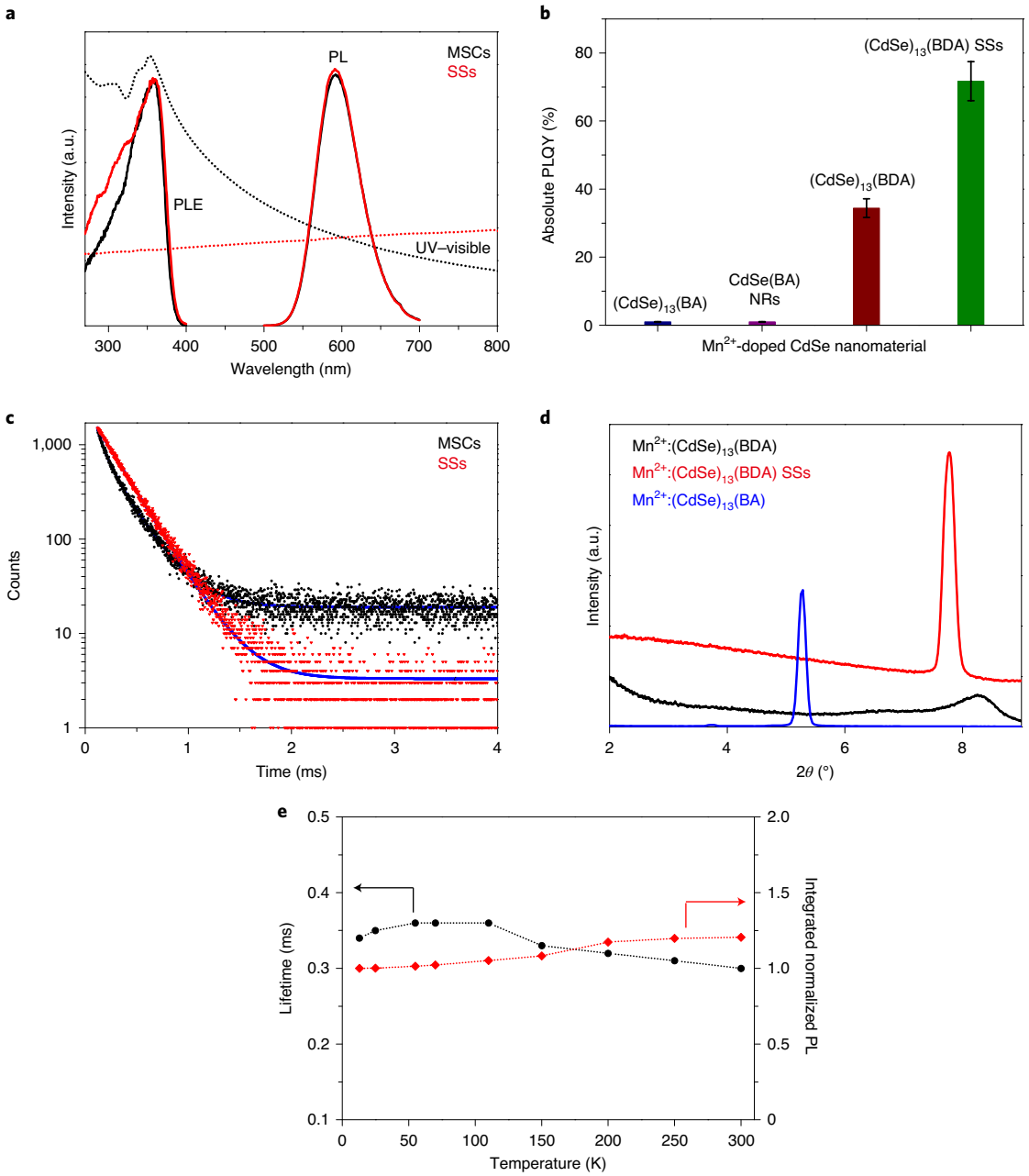

Fig. 3 | Optical and photophysical properties of MSCs and their SSs. a, UV–visible absorption (dotted lines), PL (solid lines) and PLE (solid lines) spectra of ethanol dispersions of Mn^{2+}:$(CdSe)_{13}$(BDA) MSCs (black solid and dotted lines) and their SSs (red solid and dotted lines). Owing to the predominant light scattering by SSs, the absorption features are diminished. **b**, Histograms of the absolute PLQYs of thin solid films of Mn^{2+}:$(CdSe)_{13}$(BA) MSCs, Mn^{2+}:CdSe(BA) NRs, Mn^{2+}:$(CdSe)_{13}$(BDA) MSCs and their SSs. The error bars indicate the PLQY region for three different synthesis batches of samples. **c**, Dopant-emission decay dynamics of thin solid films of Mn^{2+}:$(CdSe)_{13}$(BDA) MSCs and their SSs. Blue traces indicate corresponding fits. **d**, SAXS patterns of Mn^{2+}:$(CdSe)_{13}$(BDA) MSCs, their SSs, and Mn^{2+}:$(CdSe)_{13}$(BA) MSCs. **e**, Temperature-dependent integrated PL and PL lifetime of solid films of Mn^{2+}:$(CdSe)_{13}$(BDA) SSs.

are indeed composed of these MSCs (Fig. 3a and Supplementary Figs. 3 and 7). The Mn^{2+} content in the MSCs and SSs is 5% (atom basis) unless otherwise specified. Tracking of the SS formation with time using optical spectroscopy and electron microscopy (Supplementary Figs. 8 and 9) reveals that the in situ-formed Mn^{2+}:$(CdSe)_{13}$(BDA) MSCs continuously self-assembled to form large structures. Furthermore, the temperature is also found to play a critical role in the formation of SSs, where ~120 °C is found to be optimum for a high degree of cluster assembly (Supplementary Fig. 10).

The Mn^{2+}:$(ZnSe)_{13}$(BDA) MSCs show absorption peaks at 290 and 280 nm, blue-shifted from those of Mn^{2+}:$(CdSe)_{13}$(BDA) due to the smaller atomic size and different electronic structure of Zn from Cd (Supplementary Fig. 11). Upon SS formation, the absorption features are almost completely diminished but the sample still exhibits the corresponding PL and PLE features, confirming the intact MSCs (Supplementary Figs. 3 and 11). The Mn^{2+}:CdSe(BA) NRs grown from Mn^{2+}:$(CdSe)_{13}$(BA) MSCs display two absorption peaks at 450 and 421 nm (Supplementary Fig. 12). A slight red-shift

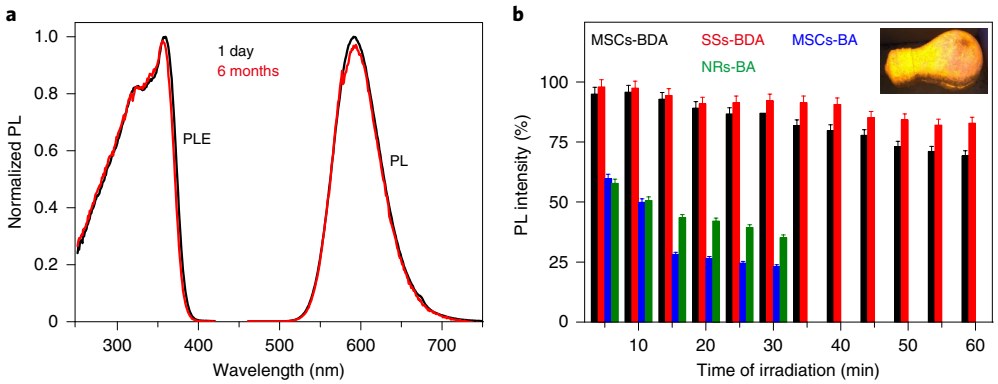

Fig. 4 | Ambient stability and photostability comparison. a, PLE and PL spectra of ethanol dispersions of Mn^{2+}:$(CdSe)_{13}$(BDA) MSCs after 1 day and 6 months of synthesis, showing high ambient stability. **b**, Monitoring the PL stability of solid films of Mn^{2+}:$(CdSe)_{13}$(BA) MSCs (blue), Mn^{2+}:CdSe(BA) NRs (green), Mn^{2+}:$(CdSe)_{13}$(BDA) MSCs (black) and their SSs (red) with time. The samples were continuously irradiated (at 350 nm for MSCs and SSs and 448 nm for NRs) for a specific duration of time in air. The error bars indicate the standard error for three repeated measurements. Inset: digital photograph of a bulb coated with Mn^{2+}:$(CdSe)_{13}$(BDA) SSs placed under a UV lamp.

of the Mn^{2+} emission from 600 to 611 nm is also in line with the modified electronic structure of NRs in comparison to MSCs. On the other hand, the Mn^{2+}:$(ZnSe)_{13}$(BA) MSCs form a mixture of uncontrolled Mn^{2+}:ZnSe and ZnSe species after colloidal thermal treatment (Supplementary Fig. 13), suggesting the unique growth pathways of both MSCs controlled by denticity of the amine ligands.

PLQY enhancement and PL decay dynamics

The absolute PLQYs of Mn^{2+}:$(CdSe)_{13}$(BA) MSCs, Mn^{2+}:CdSe(BA) NRs, Mn^{2+}:$(CdSe)_{13}$(BDA) MSCs and their SSs in the solid state are measured to investigate the effect of SS formation on the photophysical properties. Interestingly, these materials show PLQYs of <1%, <1%, ~35% and ~72%, respectively (Fig. 3b and Supplementary Table 1). Compared with MSCs ligated with monoamines (BA or *n*-octylamine (OA)), diamine (BDA)-ligated MSCs and their SSs clearly exhibit enhanced (>35-fold and >72-fold, respectively) PLQYs. Furthermore, the high Mn^{2+} doping and Zn alloying are found to decrease the PLQY probably due to the distortions in the structure of $(CdSe)_{13}$(BDA) MSCs (Supplementary Table 1).

The dopant-emission decay dynamics is investigated to gain insights into the PLQY enhancement. The Mn^{2+}:$(CdSe)_{13}$(BDA) MSCs exhibit bi-exponential PL decay curves with the two lifetime components being 305 µs (53.5%) and 84 µs (46.5%), whereas their SSs exhibit mono-exponential PL decay curves with a decay lifetime of 303 µs (Fig. 3c). The absence of multiexponential PL decay in the SSs suggests that non-radiative relaxations may be suppressed, consistent with the enhanced PLQY[45]. Importantly, small-angle X-ray scattering (SAXS) and wide-angle X-ray diffraction data (Fig. 3d and Supplementary Figs. 14 and 15) reveal that the Mn^{2+}:$(CdSe)_{13}$(BDA) MSCs in the SSs are highly ordered compared with their less-assembled state (MSCs before SS formation), indicated by sharpening of peaks with several-fold enhancement in their intensity. Furthermore, SAXS data show that the layers of MSCs are separated by a distance of the total carbon chain length of two monoamines and one diamine in the corresponding systems. This holds true for a long-chain diamine of octane-1,8-diamine (ODA) as well (Supplementary Fig. 14). The intercluster bridging by diamine ligands (depicted in Fig. 1a) is supported by Fourier transform infrared spectroscopy and X-ray photoelectron spectroscopy results with a red-shift of the $-NH_2$ stretching peaks and a blue-shift of the N 1*s* peak, respectively, from pristine diamine (Supplementary Figs. 16 and 17). Such ordered assembly of MSCs leads to the removal of surface defects (Supplementary Table 2), explaining the minimization of non-radiative relaxation pathways and PLQY enhancement[46–48].

On the other hand, Mn^{2+}:$(CdSe)_{13}$(BA) MSCs possess a high density of surface defects (Supplementary Table 3), as indicated by their bi-exponential PL decay curves with short-lifetime components corresponding to non-radiative processes (Supplementary Fig. 18), thus resulting in low PLQYs. The homogeneous distribution of the Mn^{2+}:$(CdSe)_{13}$(BDA) MSCs in the SSs further facilitates the PL enhancement, where at 1% Mn^{2+} doping, the MSCs in SSs are observed to be well delocalized (Supplementary Fig. 19). At the same dopant concentration, the Mn^{2+}:$(CdSe)_{13}$(BDA) MSCs show broad electron paramagnetic resonance signals due to inhomogeneous distribution, leading to Mn^{2+}–Mn^{2+} pairing. However, at >1% Mn^{2+} doping levels, both Mn^{2+}:$(CdSe)_{13}$(BDA) MSCs and their SSs show broad features because of the enhanced Mn^{2+}–Mn^{2+} spin coupling.

Temperature-dependent PL and PLE spectroscopies reveal the semiconductor-like behaviour of Mn^{2+}:$(CdSe)_{13}$(BDA) MSCs and those in SSs (Supplementary Fig. 20). Notably, the PL intensities and decay for the Mn^{2+}:$(CdSe)_{13}$(BDA) SSs are largely independent of temperature (Fig. 3e), suggesting a temperature-independent PLQY. The mono-exponential PL decay curves of the SSs indicate suppression of non-radiative recombination at all temperatures (Supplementary Fig. 21). Owing to the experimental inconsistencies related to the necessary deep-ultraviolet (UV) excitations, PLQYs of Mn^{2+}:$(ZnSe)_{13}$(BDA) MSCs and their SSs are not determined, but it is apparent that they exhibit highly enhanced Mn^{2+} PL by the formation of SSs. Consistently, the PL decay dynamics of Mn^{2+}:$(ZnSe)_{13}$(BDA) SSs shows an enhanced lifetime with a bi-exponential decay (Supplementary Fig. 22). It is surmised that the 2D SS of Mn^{2+}:$(ZnSe)_{13}$(BDA) is exposed one-dimensionally, leading to only partial removal of non-radiative recombination pathways.

Furthermore, the SSs of Mn^{2+}:$(CdSe)_{13}$ MSCs are synthesized by using diamines of varied carbon chain length (C_4, C_6, C_8 and C_{12}) to gain insights into factors favouring the SS formation and their effect on PLQY. With the increase in chain length of diamine, PL lifetimes and the overall size of the SSs, as well as scattering in their absorption spectra, are decreased (Supplementary Fig. 23). The PLQY of Mn^{2+}:$(CdSe)_{13}$(ODA) SSs, where the MSCs are protected by ODA ligands with intermediate carbon chain length, is decreased to ~62% (Supplementary Table 1) due to the decreased degree of SSs. A portion of unreacted MSCs with small 2D structures along with NRs are also observed in the TEM image (Supplementary Fig. 23) of SSs formed by C_{12} diamine. The concurrent appearance of the NR feature in the absorption spectrum suggests weaker binding of the longer diamine

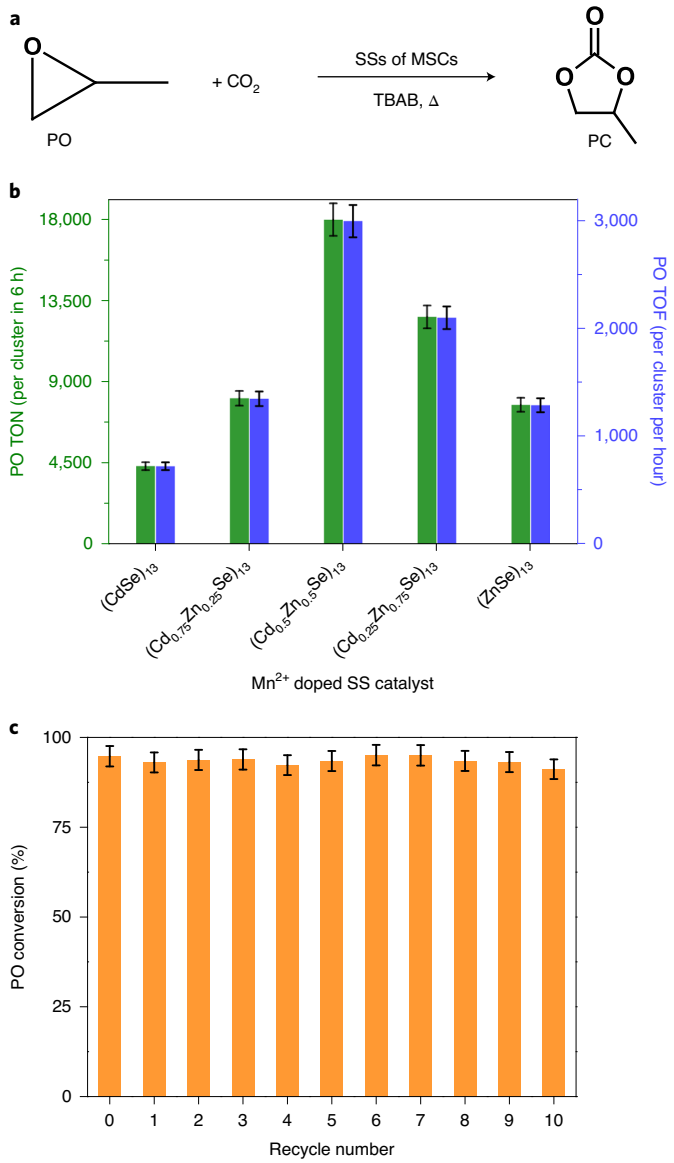

Fig. 5 | Catalytic performance of SSs of MSCs. a, Solvent-free thermo-catalytic cycloaddition of CO_2 gas with PO, forming PC in the presence of tetrabutylammonium bromide (TBAB) cocatalyst. **b**, Catalytic performance of SSs of Mn^{2+}:$(CdSe)_{13}$, Mn^{2+}:$(Cd_{0.75}Zn_{0.25}Se)_{13}$, Mn^{2+}:$(Cd_{0.5}Zn_{0.5}Se)_{13}$, Mn^{2+}:$(Cd_{0.25}Zn_{0.75}Se)_{13}$ and Mn^{2+}:$(ZnSe)_{13}$ MSCs. **c**, Recyclability of Mn^{2+}:$(Cd_{0.5}Zn_{0.5}Se)_{13}$(BDA) SSs for PO conversion. The error bars in **b** and **c** indicate the standard error for three repeated measurements.

with MSCs, which is similar to those synthesized with monoamine ligands. These experimental results show that the rigid and short ligation resulting from the short-chain-length diamine directs the reaction toward the formation of the SSs of intact MSCs. The long diamines largely separate the MSCs from one another, resulting in insignificant interlayer coupling and suppression of the SS formation. The diamine-chain-length-dependent PLE spectra of Mn^{2+}:$(CdSe)_{13}$ SSs show that with decreasing diamine chain length there is a clear red-shift in the PLE position corresponding to both the host and Mn^{2+} transition (Supplementary Fig. 24), strongly supporting enhanced coupling between interlayers of MSCs[49,50], which promotes the SS formation. As a result, SSs with a higher degree of well-ordered MSCs with rigid diamines exhibit large enhancements in the PLQY.

Stability of diamine-based MSCs and SSs

It is worth recalling that Mn^{2+}:$(CdSe)_{13}$ MSCs exhibit slightly enhanced stability compared with undoped MSCs (Supplementary Fig. 25). Therefore, here, we proceed with a comparison of the ambient stabilities of solely Mn^{2+}:$(CdSe)_{13}$ MSCs stabilized by monoamine and diamine ligands. After washing the MSCs with ethanol, the as-prepared Mn^{2+}:$(CdSe)_{13}$(BA) MSCs decomposed and grew into NR-like structures within 30 min, indicating their poor stability (Supplementary Fig. 26a). On the other hand, under the same purification treatment, the Mn^{2+}:$(CdSe)_{13}$(BDA) MSCs show unchanged absorption, PL and PLE features even after 6 months in air and at room temperature (Fig. 4a and Supplementary Fig. 26b), suggesting a dramatic improvement in ambient stability. The high stability of Mn^{2+}:$(CdSe)_{13}$(BDA) MSCs and their SSs, compared with Mn^{2+}:$(CdSe)_{13}$(BA) MSCs, is consistent with the thermal stability data (Supplementary Fig. 27), where ligand loss occurs at a higher temperature in the former BDA cases due to rigid binding. We further evaluated the photostability of various Mn^{2+}:CdSe nanomaterials by monitoring the Mn^{2+} emission by exciting them aerobically with an intense light. Within 30 min of irradiation, the PL intensities of the Mn^{2+}:$(CdSe)_{13}$(BA) MSCs and Mn^{2+}:CdSe(BA) NRs dropped by 78% and 65%, respectively (Fig. 4b). The poor photostability of monoamine-based MSCs compared with NRs is probably due to their smaller size and larger surface area, resulting in high reactivity and degradation in air. In the same time period, the Mn^{2+}:$(CdSe)_{13}$(BDA) MSCs and their SSs show only a slight PL intensity drop (13% and 7%, respectively). After prolonged irradiation, SSs and MSCs retain 83% and 69% PL, respectively, indicating the high photostability of SSs ligated by diamines. Furthermore, the as-prepared Mn^{2+}:$(CdSe)_{13}$ SSs are deposited onto surfaces, where they continue to exhibit bright orange emission upon UV excitation (Fig. 4b inset), demonstrating their potential for lighting applications, supported by their photostability and high PLQY.

Catalytic CO_2 conversion to cyclic carbonates

Benefited by the high stability of SSs of ordered atomically precise metal chalcogenide MSCs, we evaluate the catalytic performance of Lewis acidic sites (Cd^{2+} and Zn^{2+}) in a model reaction of CO_2 cycloaddition to epoxides[51]. Recently, the catalytic conversion of CO_2, the main component of fossil fuel emissions that cause global warming and ocean acidification, into environmentally friendly substances and useful chemicals has attracted tremendous attention[30,52]. Notably, organic cyclic carbonates, the products of CO_2 cycloaddition to epoxides, are important chemicals in the polymer, pharmaceutical and fine chemical industries[25,52,53]. Annually, ~40,000 tons of cyclic carbonates are being produced from CO_2 industrially[54], and achieving their facile synthesis still requires efficient and recyclable catalysts, especially working at mild reaction conditions. In addition to the strong Lewis acidity of Cd^{2+} and Zn^{2+} sites, the anticipated cooperative and efficient CO_2 adsorption on diamine-modified systems[55] and the possibility to synthesize CdZn alloy SSs (see below) with tunable metal composition and synergistic effects[30] together prompted us to perform CO_2 conversion to cyclic carbonates. The SSs of Mn^{2+}:$(CdSe)_{13}$(BDA) and Mn^{2+}:$(ZnSe)_{13}$(BDA) MSCs were screened as catalysts for the solvent-free propylene oxide (PO) reaction with CO_2 gas under mild reaction conditions (see Methods for details). Indeed, the SSs exhibit catalytic activity for propylene carbonate (PC) formation with 100% selectivity and varied PO conversions. The Mn^{2+}:$(ZnSe)_{13}$(BDA) SSs show higher PO conversion compared with Mn^{2+}:$(CdSe)_{13}$(BDA) SSs (Supplementary Fig. 28) probably due to the slightly harder cationic nature of Zn^{2+} compared with Cd^{2+}.

We envisioned that the atomic-level alloying of Zn and Cd within the size-retained MSCs could form SSs with high catalytic activity due to the synergistic interactions between these metals. To demonstrate this, we synthesized SSs of MSCs with tunable Cd and Zn

compositions (Supplementary Figs. 29–32). Catalytic results show the systematic increase of PO conversion with the increase of Zn^{2+} content, with the Mn^{2+}:$(Cd_{0.5}Zn_{0.5}Se)_{13}$(BDA) already showing nearly full conversion of PO (Supplementary Fig. 28). We further evaluate the catalytic performance of CdZn alloy clusters by calculating the turnover number (TON) for PO conversion. Remarkably, the Mn^{2+}:$(Cd_{0.5}Zn_{0.5}Se)_{13}$(BDA) SS shows the highest TON (17,964 per cluster in 6 h) and turnover frequency (TOF) (2,994 per cluster per h) for PO conversion, while the Mn^{2+}:$(Cd_{0.25}Zn_{0.75}Se)_{13}$(BDA) with higher Zn content and Mn^{2+}:$(ZnSe)_{13}$(BDA) exhibit lower performance (Fig. 5a,b). These results indicate that $Cd_{0.5}Zn_{0.5}$ is the optimal atomic ratio of Zn and Cd to guide effective synergistic effects. The observed catalytic activity in this work is quite promising as compared with the reported Lewis-acid-based catalysts for cyclic carbonate formation reaction under mild conditions (Supplementary Table 4). Furthermore, the Mn^{2+}:$(Cd_{0.5}Zn_{0.5}Se)_{13}$(BDA) SS catalyst is recyclable up to ten cycles without compromising its catalytic activity (Fig. 5c). The spectroscopy, microscopy and elemental analysis data reveal that the morphology and the composition of the SS catalysts are almost unchanged (Supplementary Figs. 33 and 34). The easy separation of the SS catalysts from the reaction products, quick assessment of the catalyst stability by visible PL using a portable UV lamp and no requirement for additional support for the catalyst loading are other benefits of the SSs. Consequently, the atomic-level alloying and tunable CdZn compositions within the intact size of the MSCs are shown to modulate the catalytic performance by atomic-level synergistic effects.

In summary, we have demonstrated a diamine-based self-assembly process to assemble metal chalcogenide MSCs Mn^{2+}:$(CdSe)_{13}$ and Mn^{2+}:$(ZnSe)_{13}$ into SSs. The rigid binding of diamines of appropriate carbon chain length plays a crucial role in not only preserving the MSCs but also guiding their assembly. On the other hand, corresponding monoamines lacking such rigidity favour the decomposition and transformation of MSCs into NRs. The SSs of MSCs displayed enhanced PLQYs up to ~72% and ambient stability for up to 6 months. Detailed spectroscopic characterization suggests that the high ordering of MSCs and the removal of surface defects are responsible for the enhanced photophysical properties. Furthermore, the SSs of Mn^{2+}:$(Cd_{1-x}Zn_xSe)_{13}$ alloy MSCs are synthesized with tunable metal compositions and synergistic effects by maintaining the original nuclearity of the MSCs. The optimal synergistic interactions in Mn^{2+}:$(Cd_{0.5}Zn_{0.5}Se)_{13}$ SSs result in excellent catalytic activity (TON: 17,964 per cluster in 6 h; TOF: 2,994 per cluster per h) and recyclability for CO_2 conversion to cyclic carbonates. We hope that these findings will stimulate semiconductor nanocluster research for advancing optoelectronic and other catalytic applications.

Online content

Any methods, additional references, Nature Research reporting summaries, source data, extended data, supplementary information, acknowledgements, peer review information; details of author contributions and competing interests; and statements of data and code availability are available at https://doi.org/10.1038/s41563-020-00880-6.

Received: 20 August 2020; Accepted: 13 November 2020;
Published online: 18 January 2021

References

1. Williamson, C. B. et al. Chemically reversible isomerization of inorganic clusters. *Science* **363**, 731–735 (2019).
2. Beecher, A. N. et al. Atomic structures and gram scale synthesis of three tetrahedral quantum dots. *J. Am. Chem. Soc.* **136**, 10645–10653 (2014).
3. Nevers, D. R. et al. Mesophase formation stabilizes high-purity magic-sized clusters. *J. Am. Chem. Soc.* **140**, 3652–3662 (2018).
4. Gary, D. C. et al. Single-crystal and electronic structure of a 1.3 nm indium phosphide nanocluster. *J. Am. Chem. Soc.* **138**, 1510–1513 (2016).
5. Kasuya, A. et al. Ultra-stable nanoparticles of CdSe revealed from mass spectrometry. *Nat. Mater.* **3**, 99–102 (2004).
6. Palencia, C., Yu, K. & Boldt, K. The future of colloidal semiconductor magic-size clusters. *ACS Nano* **14**, 1227–1235 (2020).
7. Gary, D. C., Terban, M. W., Billinge, S. J. L. & Cossairt, B. M. Two-step nucleation and growth of InP quantum dots via magic-sized cluster intermediates. *Chem. Mater.* **27**, 1432–1441 (2015).
8. Lee, J., Yang, J., Kwon, S. G. & Hyeon, T. Nonclassical nucleation and growth of inorganic nanoparticles. *Nat. Rev. Mater.* **1**, 16034 (2016).
9. Kudera, S. et al. Sequential growth of magic-size CdSe nanocrystals. *Adv. Mater.* **19**, 548–552 (2007).
10. Friedfeld, M. R., Stein, J. L., Ritchhart, A. & Cossairt, B. M. Conversion reactions of atomically precise semiconductor clusters. *Acc. Chem. Res.* **51**, 2803–2810 (2018).
11. Tan, L. et al. Structures of CdSe and CdS nanoclusters from ab initio random structure searching. *J. Phys. Chem. C* **123**, 29370–29378 (2019).
12. Dolai, S. et al. Isolation of bright blue light-emitting CdSe nanocrystals with 6.5 kDa core in gram scale: high photoluminescence efficiency controlled by surface ligand chemistry. *Chem. Mater.* **26**, 1278–1285 (2014).
13. Zhang, B. et al. Thermally-induced reversible structural isomerization in colloidal semiconductor CdS magic-size clusters. *Nat. Commun.* **9**, 2499 (2018).
14. VanWie, T., Wysocki, E., McBride, J. R. & Rosenthal, S. J. Bright cool white emission from ultrasmall CdSe quantum dots. *Chem. Mater.* **31**, 8558–8562 (2019).
15. DeGroot, M. W., Taylor, N. J. & Corrigan, J. F. Zinc chalcogenolate complexes as capping agents in the synthesis of ternary II–II′–VI nanoclusters: structure and photophysical properties of $[(N,N'\text{-tmeda})_5Zn_5Cd_{11}Se_{13}(SePh)_6(thf)_2]$. *J. Am. Chem. Soc.* **125**, 864–865 (2003).
16. Huang, X. et al. Flexible hybrid semiconductors with low thermal conductivity: the role of organic diamines. *Angew. Chem. Int. Ed.* **48**, 7871–7874 (2009).
17. Harrell, S. M., McBride, J. R. & Rosenthal, S. J. Synthesis of ultrasmall and magic-sized CdSe nanocrystals. *Chem. Mater.* **25**, 1199–1210 (2013).
18. Wang, Y. et al. Isolation of the magic-size CdSe nanoclusters $[(CdSe)_{13}(n\text{-octylamine})_{13}]$ and $[(CdSe)_{13}(\text{oleylamine})_{13}]$. *Angew. Chem. Int. Ed.* **51**, 6154–6157 (2012).
19. Levchenko, T. I. et al. Luminescent CdSe superstructures: a nanocluster superlattice and a nanoporous crystal. *J. Am. Chem. Soc.* **139**, 1129–1144 (2017).
20. Kwon, Y. et al. Evolution from unimolecular to colloidal-quantum-dot-like character in chlorine or zinc incorporated InP magic size clusters. *Nat. Commun.* **11**, 3127 (2020).
21. Wang, C. et al. Three-dimensional superlattices built from $(M_4In_{16}S_{33})^{10-}$ (M = Mn, Co, Zn, Cd) supertetrahedral clusters. *J. Am. Chem. Soc.* **123**, 11506–11507 (2001).
22. Robinson, R. D. et al. Spontaneous superlattice formation in nanorods through partial cation exchange. *Science* **317**, 355–358 (2007).
23. Talapin, D. V. et al. Dynamic distribution of growth rates within the ensembles of colloidal II–VI and III–V semiconductor nanocrystals as a factor governing their photoluminescence efficiency. *J. Am. Chem. Soc.* **124**, 5782–5790 (2002).
24. Wang, Q. & Astruc, D. State of the art and prospects in metal–organic framework (MOF)-based and MOF-derived nanocatalysis. *Chem. Rev.* **120**, 1438–1511 (2020).
25. Trickett, C. A. et al. The chemistry of metal–organic frameworks for CO_2 capture, regeneration and conversion. *Nat. Rev. Mater.* **2**, 17045 (2017).
26. Boles, M. A., Engel, M. & Talapin, D. V. Self-assembly of colloidal nanocrystals: from intricate structures to functional materials. *Chem. Rev.* **116**, 11220–11289 (2016).
27. Cao, M. et al. Porphyrinic silver cluster assembled material for simultaneous capture and photocatalysis of mustard-gas simulant. *J. Am. Chem. Soc.* **141**, 14505–14509 (2019).
28. Huang, R.-W. et al. Hypersensitive dual-function luminescence switching of a silver-chalcogenolate cluster-based metal–organic framework. *Nat. Chem.* **9**, 689–697 (2017).
29. Polgar, A. M., Weigend, F., Zhang, A., Stillman, M. J. & Corrigan, J. F. A *N*-heterocyclic carbene-stabilized coinage metal-chalcogenide framework with tunable optical properties. *J. Am. Chem. Soc.* **139**, 14045–14048 (2017).
30. Deacy, A. C., Kilpatrick, A. F. R., Regoutz, A. & Williams, C. K. Understanding metal synergy in heterodinuclear catalysts for the copolymerization of CO_2 and epoxides. *Nat. Chem.* **12**, 372–380 (2020).
31. Xia, Y. et al. Self-assembly of self-limiting monodisperse supraparticles from polydisperse nanoparticles. *Nat. Nanotechnol.* **6**, 580–587 (2011).
32. Tang, Z., Kotov, N. A. & Giersig, M. Spontaneous organization of single CdTe nanoparticles into luminescent nanowires. *Science* **297**, 237–240 (2002).
33. Levchenko, T. I. et al. Controlled solvothermal routes to hierarchical 3D superparticles of nanoscopic CdS. *Chem. Mater.* **27**, 3666–3682 (2015).
34. Guldi, D. M. et al. Versatile organic (fullerene)–inorganic (CdTe nanoparticle) nanoensembles. *J. Am. Chem. Soc.* **126**, 14340–14341 (2004).

35. Tang, Z., Zhang, Z., Wang, Y., Glotzer, S. C. & Kotov, N. A. Self-assembly of CdTe nanocrystals into free-floating sheets. *Science* **314**, 274–278 (2006).
36. Claridge, S. A. et al. Cluster-assembled materials. *ACS Nano* **3**, 244–255 (2009).
37. Boles, M. A. & Talapin, D. V. Self-assembly of tetrahedral CdSe nanocrystals: effective "patchiness" via anisotropic steric interaction. *J. Am. Chem. Soc.* **136**, 5868–5871 (2014).
38. Yang, J. et al. Chemical synthesis, doping, and transformation of magic-sized semiconductor alloy nanoclusters. *J. Am. Chem. Soc.* **139**, 6761–6770 (2017).
39. Liu, Y.-H., Wang, F., Wang, Y., Gibbons, P. C. & Buhro, W. E. Lamellar assembly of cadmium selenide nanoclusters into quantum belts. *J. Am. Chem. Soc.* **133**, 17005–17013 (2011).
40. Yu, J. H. et al. Giant Zeeman splitting in nucleation-controlled doped CdSe:Mn^{2+} quantum nanoribbons. *Nat. Mater.* **9**, 47–53 (2010).
41. Hsieh, T.-E. et al. Unraveling the structure of magic-size $(CdSe)_{13}$ cluster pairs. *Chem. Mater.* **30**, 5468–5477 (2018).
42. Wang, Y. et al. The magic-size nanocluster $(CdSe)_{34}$ as a low-temperature nucleant for cadmium selenide nanocrystals; room-temperature growth of crystalline quantum platelets. *Chem. Mater.* **26**, 2233–2243 (2014).
43. Yang, J. et al. Route to the smallest doped semiconductor: Mn^{2+}-doped $(CdSe)_{13}$ clusters. *J. Am. Chem. Soc.* **137**, 12776–12779 (2015).
44. Alkordi, M. H. et al. CO_2 conversion: the potential of porous-organic polymers (POPs) for catalytic CO_2–epoxide insertion. *J. Mater. Chem. A* **4**, 7453–7460 (2016).
45. Yang, X. et al. Temperature- and Mn^{2+} concentration-dependent emission properties of Mn^{2+}-doped ZnSe nanocrystals. *J. Am. Chem. Soc.* **141**, 2288–2298 (2019).
46. Ouyang, X. et al. DNA nanoribbon-templated self-assembly of ultrasmall fluorescent copper nanoclusters with enhanced luminescence. *Angew. Chem. Int. Ed.* **59**, 11836–11844 (2020).
47. Wu, Z. et al. Assembly-induced enhancement of Cu nanoclusters luminescence with mechanochromic property. *J. Am. Chem. Soc.* **137**, 12906–12913 (2015).
48. Lawrence, K. N. et al. Dual role of electron-accepting metal-carboxylate ligands: reversible expansion of exciton delocalization and passivation of nonradiative trap-states in molecule-like CdSe nanocrystals. *J. Am. Chem. Soc.* **138**, 12813–12825 (2016).
49. Pabla, A. S. et al. Tailoring of internal fields in InGaAs/GaAs multiwell structures grown on (111)B GaAs. *Appl. Phys. Lett.* **63**, 752–754 (1993).
50. Talapin, D. V. & Murray, C. B. PbSe nanocrystal solids for n- and p-channel thin film field-effect transistors. *Science* **310**, 86–89 (2005).
51. Samantaray, M. K. et al. The comparison between single atom catalysis and surface organometallic catalysis. *Chem. Rev.* **120**, 734–813 (2020).
52. Liang, L. et al. Carbon dioxide capture and conversion by an acid-base resistant metal-organic framework. *Nat. Commun.* **8**, 1233 (2017).
53. D'Elia, V. et al. Cooperative effect of monopodal silica-supported niobium complex pairs enhancing catalytic cyclic carbonate production. *J. Am. Chem. Soc.* **137**, 7728–7739 (2015).
54. Burkart, M. D., Hazari, N., Tway, C. L. & Zeitler, E. L. Opportunities and challenges for catalysis in carbon dioxide utilization. *ACS Catal.* **9**, 7937–7956 (2019).
55. McDonald, T. M. et al. Cooperative insertion of CO_2 in diamine-appended metal-organic frameworks. *Nature* **519**, 303–308 (2015).

Methods

Materials. Cadmium chloride ($CdCl_2$, 99.999%), zinc chloride ($ZnCl_2$, 99.999%), manganese chloride ($MnCl_2$), butane-1,4-diamine (BDA), hexane-1,6-diamine (HDA), octane-1,8-diamine (ODA), dodecane-1,12-diamine (DDA), trioctylphosphine (TOP), *n*-butylamine (BA), *n*-octylamine (OA), silver nitrate ($AgNO_3$), triphenylphosphine (PPh_3), sodium borohydride ($NaBH_4$), dichloromethane (DCM), ethanol, methanol, elemental selenium, tetrabutylammonium bromide (TBAB) and $CDCl_3$ were purchased from Sigma-Aldrich. The (±) propylene oxide (PO) was purchased from Alfa Aesar. CO gas (99.995%) was acquired from Sinjin gas. All chemicals were used as received without further purification.

Synthesis of MSCs and SSs. The Mn^{2+}:$(CdSe)_{13}$(BDA) and Mn^{2+}:$(ZnSe)_{13}$(BDA) MSCs were synthesized as following. First, a metal–diamine precursor solution was prepared by heating a mixture of 1.5 mmol of $CdCl_2$ (or $ZnCl_2$), 0.075 mmol of $MnCl_2$ and 10 ml of BDA at 120 °C for 2 h. The selenium precursor 1,4-diaminobutylammmonium selenocarbamate was prepared at 80 °C by passing CO gas for 1 h into 5 ml of BDA containing 4.5 mmol of elemental selenium. Next, the selenium precursor was injected into the metal precursor solution at 25 °C. The resulting reaction mixture was held at 25 °C for 24 h to obtain MSCs or heated at 120 °C for 24 h to obtain SSs. After that, 50 ml of ethanol containing 3 ml of TOP was added to remove excess selenium in the form of TOPSe. Finally, MSCs and their SSs were obtained by centrifugation at 5,000 r.p.m. followed by ethanol washing. The Mn^{2+}:$(Cd_{1-x}Zn_xSe)_{13}$ ($x = 0.25$, 0.5 and 0.75) alloy MSCs and their SSs were prepared by following the above procedure with the desired amounts of Zn and Cd metal precursors. Unless otherwise mentioned, the Mn^{2+} doping of MSCs and their SSs is 5% (atom basis) both in the main text and Supplementary Information.

Synthesis of MSCs and NRs. The monoamine-ligated Mn^{2+}:$(CdSe)_{13}$(BA) and Mn^{2+}:$(CdSe)_{13}$(OA) MSCs and Mn^{2+}:CdSe(BA) NRs were synthesized by replacing BDA with BA or OA in the above procedure. The MSCs and NRs were obtained by maintaining the reaction temperature at 25 °C and 70 °C, respectively, for 24 h. The Mn^{2+}:$(ZnSe)_{13}$(BA) MSCs and their grown products (indefinite nano/microstructures) were synthesized at 25 °C and 70 °C, respectively, by simply replacing the Cd^{2+} source with a Zn^{2+} source.

Synthesis of $[Ag_{18}(PPh_3)_{10}H_{16}]^{2+}$ nanoclusters. These nanoclusters were synthesized by following a previous report[56]. Typically, a $AgNO_3$ solution (20 mg in 5 ml methanol) was mixed with a PPh_3 solution (100 mg in 7 ml DCM) and stirred at 25 °C. After 10 min, 35 mg of $NaBH_4$ dissolved in 0.5 ml deionized water was added. Upon continuous stirring of the reaction solution for 6 h, the $[Ag_{18}(PPh_3)_{10}H_{16}]^{2+}$ nanoclusters were formed.

Identification of surface defects. The Mn^{2+}:$(CdSe)_{13}$(BDA) SSs and Mn^{2+}:$(CdSe)_{13}$(BA) MSCs (5 mg each) were separately dispersed in ethanol. To these dispersions, the as-prepared $[Ag_{18}(PPh_3)_{10}H_{16}]^{2+}$ solution (4 ml each) was added under an argon atmosphere. After 4 h of gentle stirring, the MSCs and SSs were separated by centrifugation and used for elemental analysis by HAADF-STEM EDS. The large number of surface defects of MSCs is reflected in the large uptake of the Ag nanoclusters.

PLQY measurements. The solid-state absolute PLQYs were acquired using an Edinburgh FLS1000 Fluorometer equipped with an integrating sphere, which was calibrated with standard dyes with known PLQYs. The samples dispersed in ethanol were drop cast onto glass substrates and dried under ambient conditions. The reported quantum yields are the average values from samples synthesized from three separate batches.

Photostability test. Photostability experiments were conducted on thin solid films of the samples on glass substrates, obtained by drop casting ethanol dispersions followed by ambient drying. The samples were irradiated for specific durations by fixing excitation at 350 nm, slit excitation bandwidth at 20 nm, emission bandwidth at 10 nm and dwelling time at 0.2 s.

Catalytic tests of SSs. The catalytic activity of SSs of MSCs for cycloaddition of CO_2 with epoxide was evaluated using a 150 ml Parr stainless steel reactor equipped with a magnetic stirrer and a heater. In a typical reaction, the specific amount of SS catalyst, 3 ml of PO and 100 mg of TBAB cocatalyst were transferred to the reactor, which was subsequently charged with 3 bar CO_2 and heated at 70 °C for the desired time. After that, the reactor was cooled by using an ice bath and the unreacted CO_2 gas was released. About 30–50 µl of the reaction mixture was used for proton nuclear magnetic resonance spectroscopy (^{1}H NMR) for calculating the PO conversion. ^{1}H NMR spectroscopy indicated 100% selectivity for the cyclic carbonate for all the SS catalysts. For screening the activity of various catalysts and TON experiments, 50 mg and 3.8–5.3 mg catalyst, respectively, are used. For the catalyst recycling study, 25 mg of Mn^{2+}:$(Cd_{0.5}Zn_{0.5}Se)_{13}$(BDA) SS was used initially. After every cycle, the catalyst was separated by centrifuging at 8,000 r.p.m. for 6–8 min. The solid was washed two times with methanol and vacuum dried for subsequent use.

TON and TOF calculations. The TON was calculated for the PO conversion by dividing the total mmol of PO converted by the total mmol of surface metal atoms, which was estimated by inductively coupled plasma atomic emission spectroscopy. The actual number of surface metal atoms was unknown due to the lack of the atomic structure of MSCs. Therefore, it is reliable to calculate the TON per cluster by multiplying the number obtained above with 13 (the number of metal atoms in a cluster). The TOF was obtained by dividing the TON by time (h).

Data availability

Source data are provided with this paper. Image datasets in the main text and all the data in the Supplementary Information are available from the corresponding author upon reasonable request.

References

56. Bootharaju, M. S. et al. A new class of atomically precise, hydride-rich silver nanoclusters co-protected by phosphines. *J. Am. Chem. Soc.* **138**, 13770–13773 (2016).

Acknowledgements

T.H. acknowledges the financial support by the Research Center Program of the IBS (IBS-R006-D1) in Korea. D.R.G. acknowledges support from the US National Science Foundation (NSF) through the UW Molecular Engineering Materials Center, a Materials Research Science and Engineering Center (DMR-1719797), and through project DMR-1807394. This research was also supported by the Clean Energy Institute at the University of Washington.

Author contributions

W.B., M.S.B. and T.H. conceived the research. W.B. and M.S.B. designed the experiments. W.B., M.S.B., K.M.W. and S.L. performed experiments and analysed the results. K.M.W. determined PLQY values and performed temperature-dependent PL and lifetime experiments. M.S.B. and W.B. performed catalytic CO_2 conversion. S.L. conducted the HAADF-STEM and EDS analysis. W.B., M.S.B., K.M.W., S.L., D.R.G. and T.H. wrote the manuscript. T.H. supervised the project. All authors commented on the manuscript.

Competing interests

The authors declare no competing interests.

Additional information

Supplementary information is available for this paper at https://doi.org/10.1038/s41563-020-00880-6.

Correspondence and requests for materials should be addressed to T.H.

Peer review information *Nature Materials* thanks Raffaella Buonsanti and the other, anonymous, reviewer(s) for their contribution to the peer review of this work.

Reprints and permissions information is available at www.nature.com/reprints.